Journal of Molecular Catalysis A: Chemical 327 (2010) 38–44

Contents lists available at ScienceDirect

Journal of Molecular Catalysis A: Chemical

journal homepage: www.elsevier.com/locate/molcata

In situ DRIFT study of photocatalytic degradation of gaseous isopropanol over $BiVO_4$ under indoor illumination

Chao-Ming Huang[a,*], Guan-Ting Pan[b], Po-Yang Peng[c], Thomas C.-K. Yang[b]

[a] Department of Environmental Engineering, Kun Shan University, Yung Kang City, Tainan, Taiwan
[b] Department of Chemical Engineering and Biotechnology, National Taipei University of Technology, Taipei, Taiwan
[c] Graduate School of Green Materials, Kun Shan University, Yung Kang City, Tainan, Taiwan

ARTICLE INFO

Article history:
Received 26 February 2010
Received in revised form 13 May 2010
Accepted 18 May 2010
Available online 24 May 2010

Keywords:
$BiVO_4$
Visible-light-driven photocatalyst
Surface hydroxyl groups

ABSTRACT

Visible-light-driven bismuth vanadate photocatalysts were synthesized using a homogeneous co-precipitation process. X-ray diffraction (XRD) results reveal that the obtained powders consisted of monoclinic $BiVO_4$. Surface characterizations by XPS and diffuse reflectance infrared Fourier transform spectroscopy (DRIFTS) confirm the presence of surface hydroxyl groups on $BiVO_4$. The effect of adsorption ability on photocatalytic activity of $BiVO_4$ was investigated by isopropanol (IPA) adsorption and DRIFTS. All $BiVO_4$ samples exhibited a higher level of activity than that of a commercial TiO_2 photocatalyst (P25). The FTIR spectra verifying the high photocatalytic performance of $BiVO_4$ can be attributed to the rich surface hydroxyl groups that favor the high adsorption of IPA. The sample synthesized at 90 °C for 24 h (BV24) exhibits the best photocatalytic activity as evaluated using the apparent rate constant for initial photodegradation of gaseous IPA and the mineralization yield after long-term light irradiation. For an irradiation time of 720 min, the mineralization yields of IPA were 88% and 41% for BV24 and P25, respectively. This high visible-light photoactivity was ascribed to high adsorption ability, high crystallization, and large surface hydroxyl groups.

1. Introduction

Visible-light active photocatalysts have been studied extensively for environmental purification and for splitting water into H_2 and O_2. Recently, a band structure control method has been applied to design non-TiO_2-based visible-light active photocatalysts. For example, $BiVO_4$ has been recognized as a visible-light active photocatalyst for water splitting and pollutant decomposing under visible-light illumination. The photocatalytic performance of $BiVO_4$ strongly depends on its crystalline phase. Kudo reported that $BiVO_4$ with a monoclinic structure had good photocatalytic activity for O_2 evolution from an aqueous silver nitrate solution under visible-light irradiation [1]. Kohtani et al. demonstrated that monoclinic $BiVO_4$ can be used to degrade the 4-nonylphenol of an endocrine disrupter under visible-light irradiation [2]. Several methods have been reported for the preparation of monoclinic $BiVO_4$, such as solid-state reaction, hydrothermal treatment, solution combustion synthesis method, and co-precipitation [3–9]. Ke et al. synthesized $BiVO_4$ using a co-precipitation method with further calcination treatment (below 600 °C) to provide optimal monoclinic $BiVO_4$, proposing a facile method to combine surface area and crystalline confinement of the photocatalyst with better photoactivity [10].

To enhance the photocatalytic activity of the host $BiVO_4$, the transition metal and noble metal doping have been reported previously by several investigators [4,11–18]. Both enhancement as well as depletion in activity has been observed by metal doping in $BiVO_4$. Recently, the rare earth-loaded $BiVO_4$ (RE^{3+}–$BiVO_4$, RE = La, Ce, Ho, Yb, Eu, Sm, Nd and Gd) were synthesized to evaluate the photocatalytic activity; only 8% Gd–$BiVO_4$ had higher activity than that of $BiVO_4$ [19]. The detrimental effect of metal doped or metal oxides loaded was found for the modification of $BiVO_4$. It has been reported the low photocatalytic activity of pure $BiVO_4$ is due to its poor adsorption ability and difficult migration of electron–hole pairs [12,13]. The difficult migration of electron–hole pairs in loading method can be improved by the appropriate match of the band edge positions between loaded metal oxide and $BiVO_4$. However, little attention has been taken to investigate the effect of adsorption ability on photocatalytic activity of $BiVO_4$. Several studies have indicated that the surface hydroxyl groups act as active sites for pollutant adsorption [20–23]. Yet none of the previous research on $BiVO_4$ has been focused on the correlation of the surface hydroxyl groups with adsorption ability of $BiVO_4$.

In view of the importance of surface chemistry characterization, the surface hydroxyl groups of monoclinic $BiVO_4$ photocatalysts are investigated in the present study using diffuse reflectance infrared

* Corresponding author at: No. 949 Da-Wan Rd., Yung Kang City, Tainan 710, Taiwan. Tel.: +886 6 2050359; fax: +886 6 2050540.
E-mail address: charming@mail.ksu.edu.tw (C.-M. Huang).

1381-1169/$ – see front matter © 2010 Elsevier B.V. All rights reserved.
doi:10.1016/j.molcata.2010.05.009

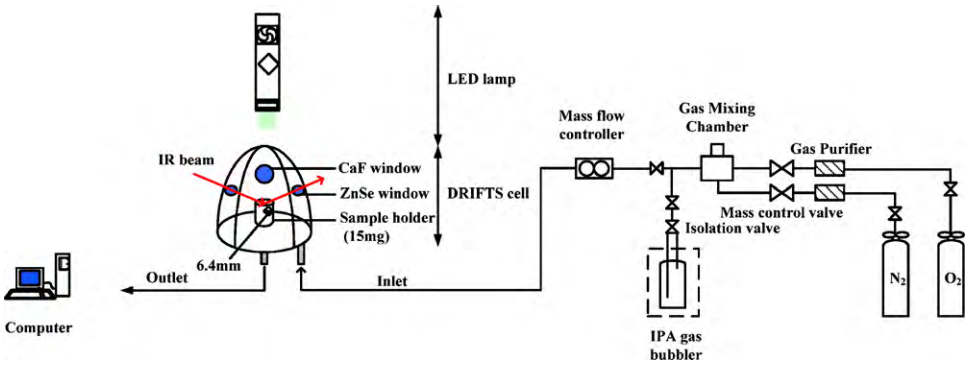

Fig. 1. Schematic diagram of in situ DRIFTS-MS system.

Fourier transform spectroscopy (DRIFTS). DRIFTS is one of the most frequently used tools for simultaneously obtaining information concerning the reaction and the characteristics of the catalyst surface. It was found that surface hydroxyl groups played a crucial role in the adsorption of isopropanol (IPA) and initial photocatalytic efficiency. The abundant amounts of surface hydroxyl groups and a high degree of monoclinic crystallinity could assuredly improve the photocatalytic activity of pure $BiVO_4$.

2. Experimental procedure

2.1. Catalyst synthesis

$BiVO_4$ was synthesized using a co-precipitation process. Bismuth nitrate pentahydrate ($Bi(NO_3)_3{\cdot}5H_2O$) and ammonium metavanadate (NH_4VO_3) were used as the bismuth and vanadium precursors, respectively. A typical synthesis process was conducted as follows: first, 0.01 mol of NH_4VO_3 was dissolved in de-ionized water at 70 °C (50 ml) to form a transparent solution, which was then cooled to room temperature; 0.01 mol of $Bi(NO_3)_3{\cdot}5H_2O$ was added to 50 ml of 1.0 M HNO_3 under magnetic stirring to form a transparent solution. The alkaline vanadate solution was then added dropwise to the acidic bismuth solution under constant stirring. After 30 min of stirring, the pH of the resulting solution was adjusted to around 5.0 using ammonia solution. Finally, the resulting solution was heated to 90 °C and then maintained for various durations under continuous stirring. The heating times were set at 6, 12, 24, 36, and 48 h for samples denoted as BV6, BV12, BV24, BV36, and BV48, respectively. The color of the solution changed from pale orange-yellow to vivid yellow. After reaction, the cooled precipitation was filtered, washed with de-ionized water, dried at 80 °C for 12 h, and calcined at 500 °C for 4 h.

2.2. Sample characterization

The X-ray diffraction (XRD) patterns were obtained using an X-ray diffractometer (PANalytical X'Pert PRO) with Cu radiation ($\lambda = 0.15418$ nm) in the 2θ range of 10–60°. The binding energies of Bi, V, and O were measured at room temperature using an X-ray photoelectron spectroscope (Kratos Axis Ultra DLD, Al Kα source). The peak positions of each element were corrected using the C 1s peak at 285.0 eV of the surface adventitious carbon. A Raman spectrometer (Ventuno, Jasco) was also applied to identify the structure of the prepared samples. Infrared spectra of the surface hydroxyl group of the catalyst surface were collected using a DRIFTS system with an FTIR spectrophotometer (PerkinElmer, spectrum GX). The DRIFTS system included a praying mantis diffuse reflectance accessory (Harrick Scientific, DRP-PE9), a controlled high temperature and low pressure reaction cell (Harrick Scientific, HVC-DRP-3), and an automatic temperature controller (ATC-024-1). Prior to the IR measurements, the samples were pre-heated under vacuum and N_2 flow (30 ml/min) was introduced simultaneously, from room temperature to 250 °C, held at 250 °C for 30 min, and then cooled to 30 °C. DRIFT spectra were collected in the range of 2600–4000 cm^{-1} for surface hydroxyl groups. The measurements were converted to the Kubelka–Munk mode and some of the selected IR peaks were deconvoluted into several Gaussian curves to obtain the peak area information. UV–vis spectra were collected using a spectrophotometer (Jasco V-500) equipped with an integrated sphere assembly over the range of 300–700 nm. The specific surface areas of as-prepared powders were measured by nitrogen adsorption/desorption using the Barrett–Emmett–Teller (BET) method (Micromeritics ASAP 2020).

2.3. Photocatalytic activity evaluation with mass spectrometry

Photocatalytic activities of the samples were determined using the photodegradation of IPA under visible-light irradiation using batch and continuous flow systems. For the single-pass continuous flow photo-reactor, 0.05 g of photocatalyst powder was evenly dispersed as a thin layer on an annular crystal tube [24]. Prior to the experiments, the samples were pre-treated at 150 °C for 30 min in dry N_2 (flowing at 100 ml/min), and then cooled to 30 °C. The reactant mixture (20 ml/min) was prepared by introducing oxygen gas, continuously bubbling, through the flask with IPA at ambient temperature, yielding a saturation concentration of ca. 160 ppmv. After the reactant mixture was purged through the photo-reactor in the dark for 60 min to achieve gas–solid adsorption equilibrium, a commercial white fluorescent lamp (TOA, FL10D-EX) was turned on. The major peaks of the white fluorescent lamp were observed at 435, 488, 545, 587 and 611 nm; the photon flux was 3.98×10^{-7} Einsteins/(s L). A constant amount of VOC vapor was periodically withdrawn from the sampling port and injected into the MS to determine the gas composition.

To determine the interaction of IPA with the photocatalysts, in situ DRIFTS was used to detect the IPA in the adsorbed form on the catalyst surface. For the batch system, after degassing, the IPA (160 ± 5 ppm) was introduced into the DRIFT cell at room temperature in the dark for 60 min. The valve used to supply the IPA vapor was then closed. A visible-light source, an LED lamp (NICHIA) with a wavelength ranging from 430 to 620 nm was used. The light was directed toward the top of the DRIFTS cell by an optical cable. The photon intensity was 4 mW/cm^2 at 2 cm away from the tip of the wand. The spectra were recorded under both darkness and illumination. A schematic diagram of the in situ micro-reactor, the diffuse reflectance accessory used to reflect the time evolution of the infrared spectrum, and the supply of VOC is shown in Fig. 1.

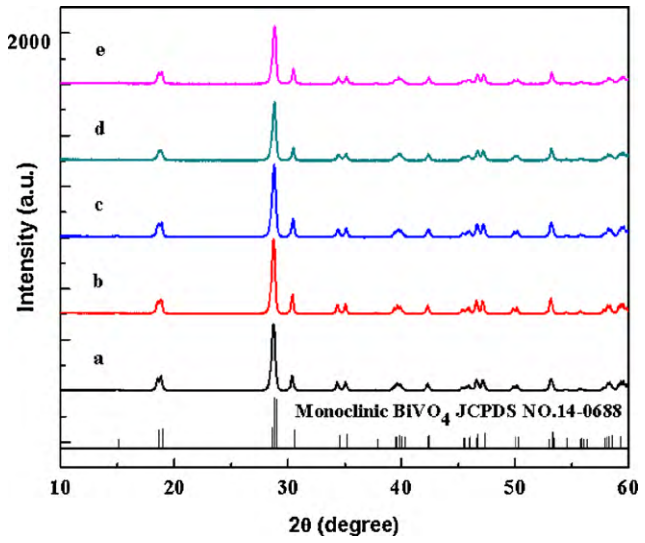

Fig. 2. XRD patterns of $BiVO_4$: (a) BV6, (b) BV12, (c) BV24, (d) BV36, and (e) BV48.

3. Results and discussion

3.1. Crystal phase analyses

Fig. 2 shows the XRD patterns of $BiVO_4$ samples synthesized at 90 °C for various durations followed by calcination treatment. Since the XRD patterns of tetragonal $BiVO_4$ are similar to those of monoclinic $BiVO_4$, the difference in the XRD patterns between tetragonal and monoclinic $BiVO_4$ is determined by whether a peak at $2\theta = 15°$ and the splitting of peaks at 18.5°, 35°, and 46° exist. Fig. 2 shows that no peaks correspond to the above-mentioned tetragonal phase. All diffraction patterns of the co-precipitated products can be indexed to monoclinic $BiVO_4$ (JCPD No. 14-0688), with no other peaks of other phases or impurities detected. The corresponding crystallite sizes of BV6, BV12, BV24, BV36, and BV48 based on Scherrer's equation were 104, 104, 52, 42, and 35 nm, respectively.

$BiVO_4$ was confirmed as a constituent of the sample by Raman spectra, as shown in Fig. 3. For all samples, the spectrum was dominated by an intense Raman band at around 822 cm^{-1}, assigned to the symmetric V–O stretching mode, and a weak shoulder at around 707 cm^{-1}, assigned to the antisymmetric V–O stretching. The peaks at 368 and 335 cm^{-1} were assigned to the symmetric and antisymmetric bending vibration of the VO_4 tetrahedra, respectively, and the peak at 214 cm^{-1} can be attributed to the external modes (rotation/translation). When the reaction time was increased to 36 h, the most intense band slightly shifted to the lower wavenumber, from 822 to 818 cm^{-1}, indicating that the average short-range symmetry of the VO_4 tetrahedra becomes more regular with synthesis time [25,26]. The positions and the full width at half maximum (FWHM) for the most intense Raman band at about 822 cm^{-1} were determined using Lorentzian curve fitting. The values of FWHM increase with increasing reaction time (results not shown). Since the Raman widths are related to the degree of crystallinity, defects and disorders, and particle size, the Raman results indicate that the samples prepared for shorter reaction durations have less symmetric VO_4 tetrahedra than those prepared for longer reaction durations. Therefore, the samples prepared for less than 36 h (BV6, BV12, and BV24) have better crystallinity and fewer defects than those prepared for longer durations (BV36 and BV48). As shown in Fig. 2, the intensities of the diffraction peaks for $BiVO_4$ increased when the reaction time was increased to 24 h, while XRD intensities considerably decreased. According to the Raman analysis, this dependence can be attributed to the formation of crystal defects, which resulted in a decrease in the crystallinity of $BiVO_4$.

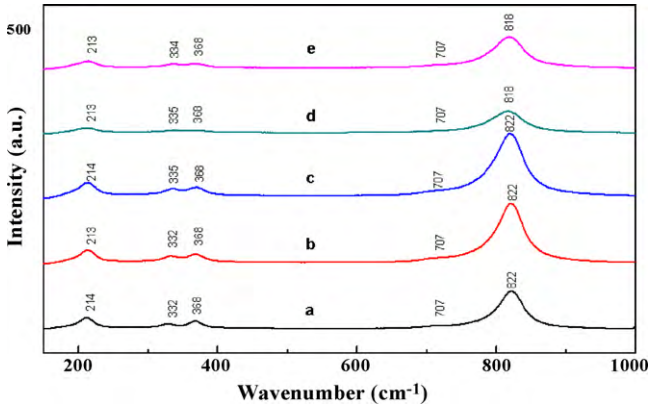

Fig. 3. Raman spectra of $BiVO_4$ samples: (a) BV6, (b) BV12, (c) BV24, (d) BV36, and (e) BV48.

3.2. Morphology

Fig. 4 shows the SEM images of the powder samples prepared by co-precipitation of aqueous solution at various synthesis times, followed by calcination at 500 °C for 4 h. All samples are sphere-like shape with a smooth surface and the size of the particles is in the range of 100–250 nm. It can be seen that synthesis time has obvious effect on the sample morphology. As shown in Fig. 4a and b, the samples synthesized at the shorter synthesis times showed the ovate-shape particles and the crystallites were connected to form large-size aggregates. The $BiVO_4$ samples, synthesized at synthesis times longer than 24 h, are composed of aggregates of small crystals (seen in Fig. 4c–e). The crystallite size of BV sample estimated by the Scherrer equation is only 35–104 nm, which is smaller than the one visualized by SEM. The crystallite size calculated from XRD results refers to the full width at half maximum of diffraction peak of crystalline and not to the physical grain size, which is visualized on the micrographics.

3.3. UV–vis diffusion reflectance spectra (UV–vis DRS)

The DRS spectra of as-prepared BV samples are shown in Fig. 5. All the samples exhibit the characteristic absorption spectra of monoclinic $BiVO_4$ with a steep sharp band shape. The onset positions of absorption edges for the samples prepared for various durations are all approximately at 515 nm, corresponding to the bandgap energy of 2.4 eV of the monoclinic $BiVO_4$ [27,28].

3.4. Activity evaluation of BV samples under white fluorescent lamp irradiation

Fig. 6 shows the effect of synthesis time on the photocatalytic decomposition of IPA over $BiVO_4$ samples under visible-light irradiation. As can be seen, BV24 has the highest photocatalytic activity. The activity decreased for samples with synthesis times longer than 24 h. Raman analysis shows that the low photocatalytic activity of BV48 might be due to the formation of crystal defects. Such defects may act as recombination centers that capture the photogenerated carriers, leading to a decrease of photoactivity [13]. The degradation data of IPA in the early stage were fitted to a pseudo-first-order model, namely, $\ln(C_0/C) = k_{app}t$ (where C_0 and C are the concentration of IPA at reaction times 0 and t, respectively, and k_{app} is the apparent rate constant). The apparent rate constants and the correlation coefficients (R^2) of the fitting are shown in Table 1. The R^2 values are all close to 1.0, implying that the pseudo-first-order kinetic model is suitable for the experimental data.

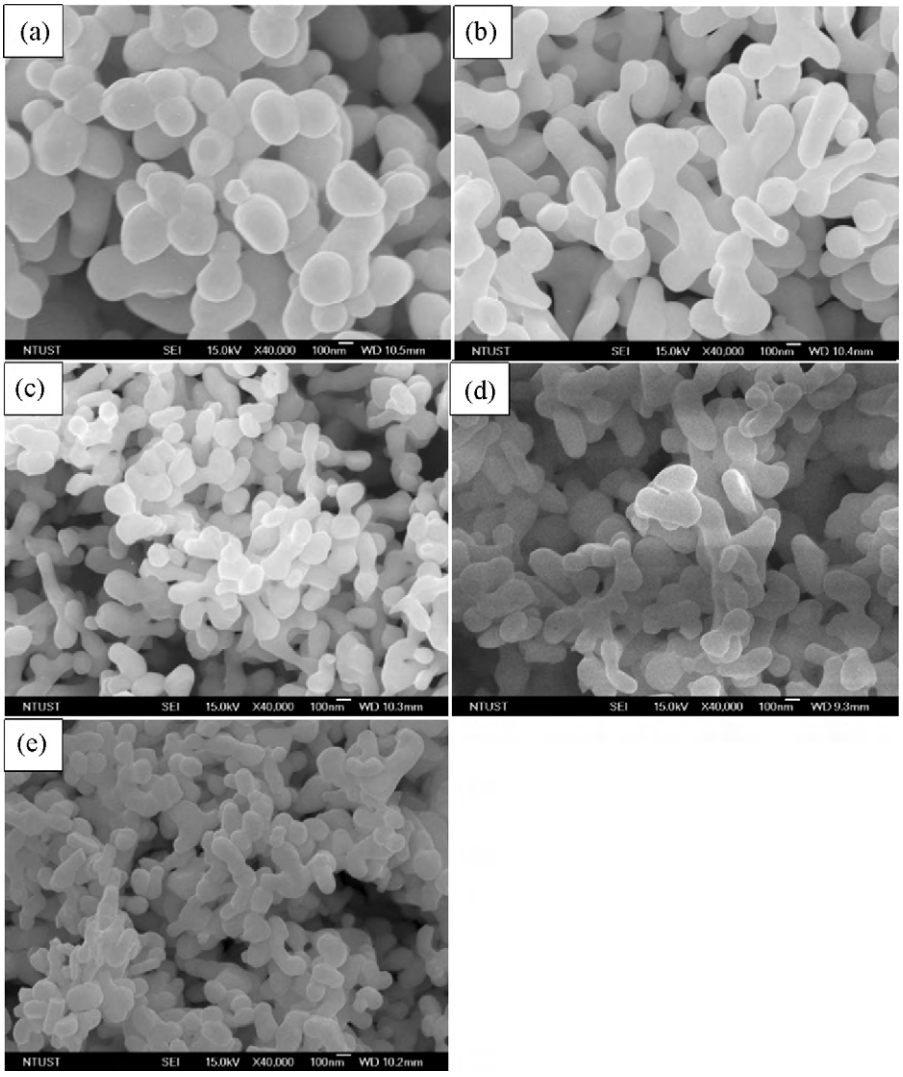

Fig. 4. SEM micrographs of $BiVO_4$: (a) BV6, (b) BV12, (c) BV24, (d) BV36, and (e) BV48.

The apparent rate constant decreased in the following sequence: BV24 > BV12 > BV36 > BV6 > BV48 > P25. The apparent rate constant of BV24 was about 2.5 times higher than that of P25. Numerous materials with the short-term ability of photodecomposing VOCs have been investigated, but few studies have been conducted on the long-term mineralization efficiencies of photocatalysts [29–31]. Only the decrease of the IPA concentration in the early stage is not sufficient for the comparison of photocatalytic activity; therefore,

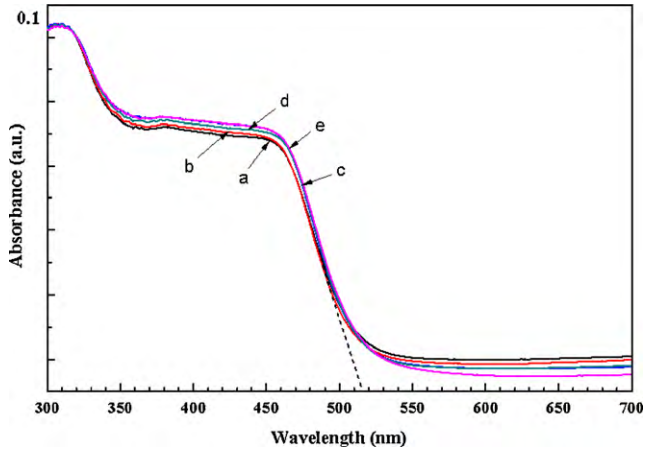

Fig. 5. UV–vis DRS of $BiVO_4$ samples: (a) BV6, (b) BV12, (c) BV24, (d) BV36, and (e) BV48.

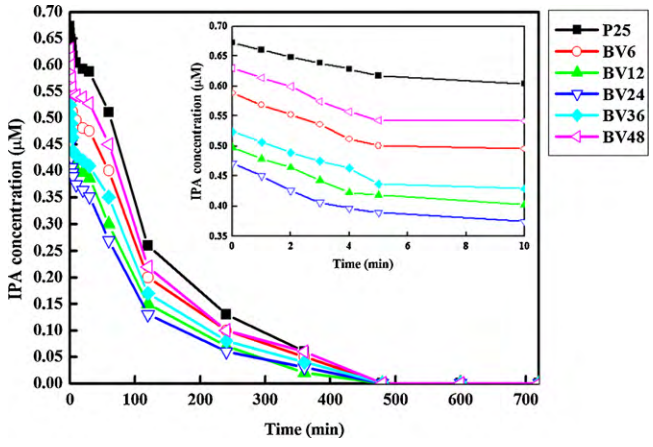

Fig. 6. Gaseous IPA concentration as a function of irradiation time using $BiVO_4$ and P25 samples. The insert shows degradation curves of gaseous IPA from $t = 0$ to $t = 10$ min under visible-light irradiation.

Table 1
Apparent rate constant and mineralization performance of BV samples and P25 under 720 min of irradiation.

Sample	Apparent rate constant (min^{-1})	Mineralization yield (%)	R^2
P25	0.017	41	0.998
BV6	0.032	65	0.994
BV12	0.037	81	0.982
BV24	0.043	88	0.968
BV36	0.034	78	0.986
BV48	0.030	61	0.992

to evaluate the long-term photoactivity of BV and P25 samples, the amount of CO_2, a final decomposition product of gaseous IPA, was measured. The mineralization yield of gaseous IPA is defined as [32]:

$$\text{mineralization}\,(\%) = \frac{1/3[CO_2]_{\text{production}}}{[CH_3CHOHCH_3]_{\text{original}}} \times 100$$

For a 100% mineralization yield, 3 mol of carbon dioxide are formed from each mole of IPA. The results of mineralization yield under visible-light illumination are listed in Table 1. For an irradiation time of 720 min, the mineralization yields of IPA were 88% and 41% for BV24 and P25, respectively. The CO_2 measurements reveal the high efficiency of mineralization over BV24 under white fluorescent lamp irradiation. Based on the short-term decrease of IPA concentration and the long-term increase of CO_2 concentration, the photocatalytic ability of the BV24 sample is significantly superior to that of P25.

3.5. XPS studies

To identify the chemical states of the atoms in BV samples, X-ray photoelectron spectroscopy was applied. The overall XPS spectra for all BV photocatalysts were similar. The XPS spectra of the three elements of the BV24 sample are shown in Fig. 7. The binding energies located at 164.1 and 158.8 eV were assigned to the Bi $4f_{5/2}$ orbital and the Bi $4f_{7/2}$ orbital, respectively (Fig. 7a) [13]. The V 2p orbits have splitting peaks at 524.4 and 516.4 eV (Fig. 7b), which are corresponding to the V $2p_{1/2}$ orbital and the V $2p_{3/2}$ orbital, respectively. A narrow peak located at 529.4 eV can be attributed to the lattice oxygen of crystalline $BiVO_4$ and an additional band around 531.4 eV is related to the chemisorbed H_2O or hydroxyl groups on the surface (Fig. 7c) [33].

3.6. Surface hydroxyl groups over BV samples

The photodegradation studies of gaseous IPA indicate that the BV samples have a wide range of behavior, based on the k_{app} and mineralization data in Table 1. It is well known that either the adsorption process or the surface reaction is the rate-determining step for catalytic reactions; therefore, the photocatalytic reaction strongly depends on the crystalline structure, specific surface area, and adsorption/desorption characteristics. For adsorption/desorption characteristics, the equilibrium adsorption amount of volatile organic compound in the dark provides a qualitative indication of the adsorption affinity between VOC and the photocatalyst. The adsorption amounts of IPA on the samples, at the beginning of the photocatalytic reaction, decreased in the following sequence: BV24 > BV12 > BV36 > BV6 > BV48, as shown in Fig. 6. In general, a higher surface area of the adsorbent leads to a higher adsorption capacity. The specific surface areas of BV6, BV12, BV24, BV36, and BV48 are 3.4, 4.0, 5.0, 6.7, and 7.5 $m^2\,g^{-1}$, respectively. Obviously, the BV48 showed much lower adsorption capability than that of BV24 samples, implying that a large surface area did not favor the adsorption of IPA. It appears that IPA adsorption is not correlated with the surface area of $BiVO_4$ in this study. Therefore, parameters other than surface area need to be investigated. The most important parameter is the surface chemistry of the adsorbents used. A literature survey indicates that the surface OH groups provide the adsorption centers for reagents and/or products and can be the precursors of hydroxyl radicals responsible for many photocatalytic reactions [20–23]. The existence of the OH group was detected over BV24, as shown in Fig. 7. To determine whether the surface hydroxyl groups of BV samples affect the adsorption of IPA and degradation abilities, in situ DRIFTS experiments were conducted. Before DRIFTS measurements, the samples were heated to 250 °C to remove adsorbed water. Fig. 8 shows the FTIR spectra of BV samples in the range 4000–2600 cm^{-1}. Within this range, two broad strong bands and

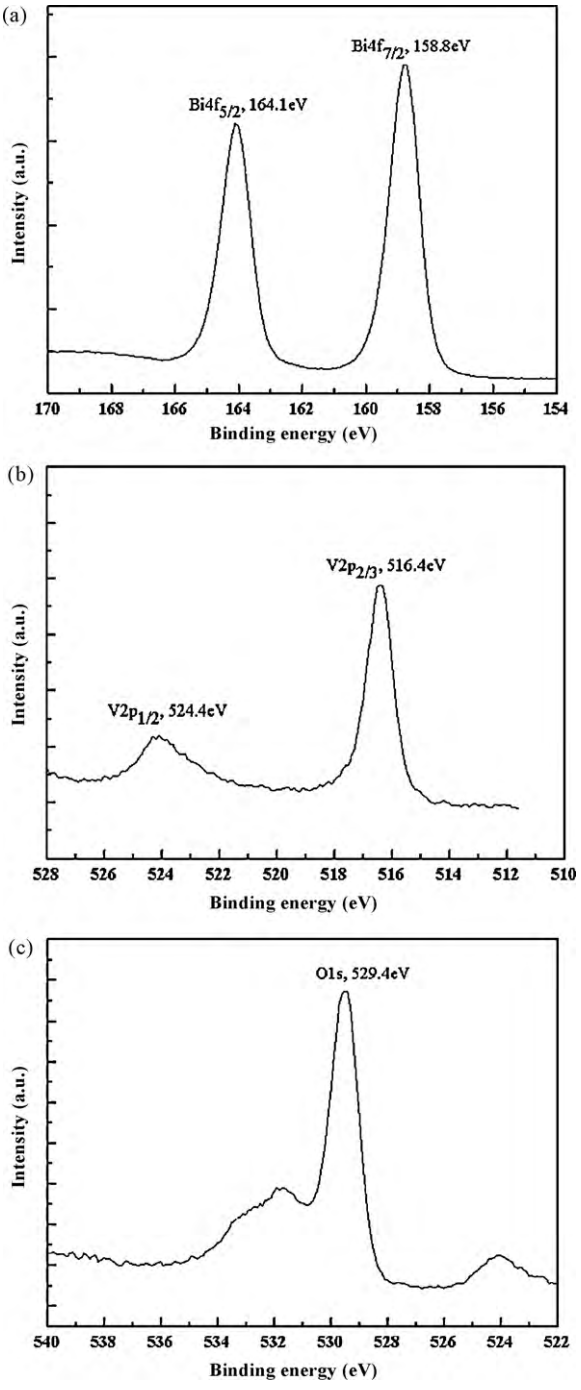

Fig. 7. XPS spectra of BV24 samples: (a) Bi 4f, (b) V 2p, and (c) O 1s.

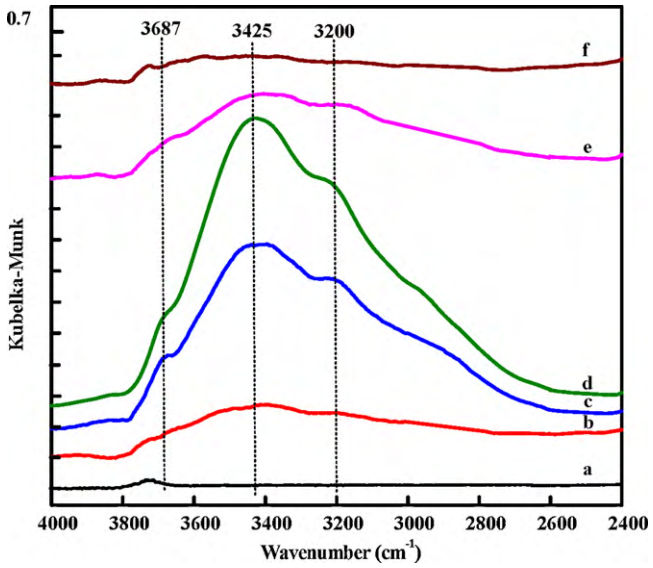

Fig. 8. Infrared spectra of OH groups on $BiVO_4$ samples heated at 250 °C: (a) BV6, (b) BV12, (c) BV24, (d) BV36, and (e) BV48.

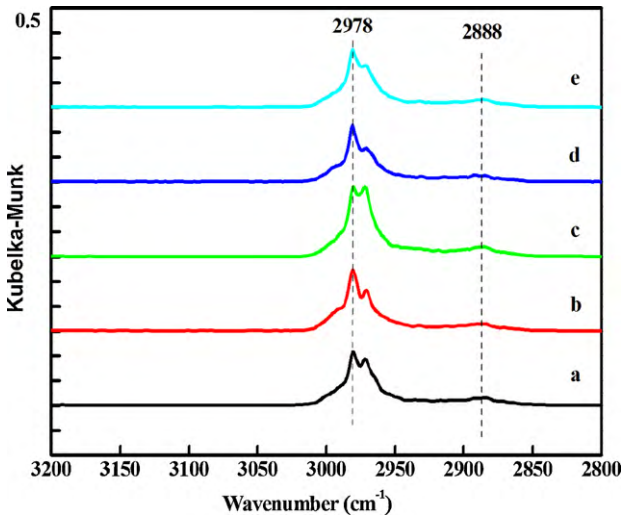

Fig. 9. DRIFT spectra of the ν(CH) mode of methyl groups of adsorbed IPA on $BiVO_4$ samples: (a) BV6, (b) BV12, (c) BV24, (d) BV36, and (e) BV48 after 30 min of darkness.

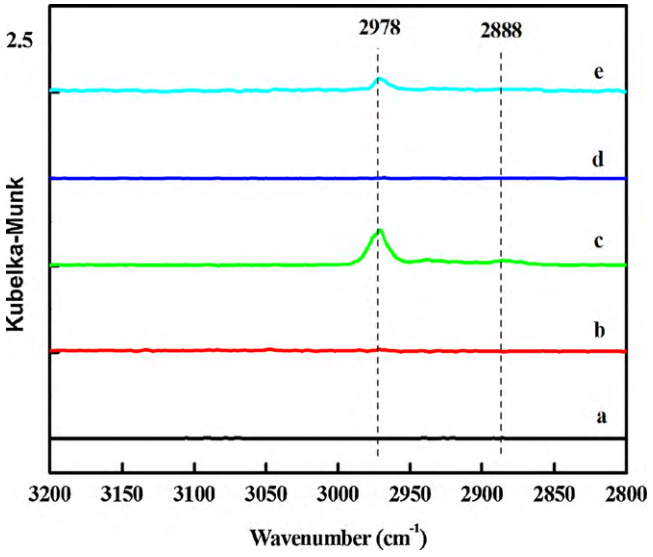

Fig. 10. DRIFT spectra of the ν(CH) mode of methyl groups of adsorbed IPA on $BiVO_4$ samples: (a) BV6, (b) BV12, (c) BV24, (d) BV36, and (e) BV48 after 20 min of illumination.

one weak band corresponding to surface hydroxyl groups can be seen. For a quantitative comparison of OH groups, a deconvolution procedure was applied to BV samples, which resulted in three Gaussian curves based on the IR assignments of OH groups (at 3200, 3425, and 3687 cm^{-1}) reported in the literature. The peak at 3200 cm^{-1} is the typical OH group chemically adsorbed on the surface of a photocatalyst [34]; the peaks at 3425 and 3687 cm^{-1} can be assigned to hydrogen bonded O–H stretching vibration [35] and linear ν(OH) [36], respectively. The amounts of various OH groups on the BV samples can be obtained by integrating the three individual curves, as shown in Table 2. The amount of OH groups decreases in the order of BV24 > BV12 > BV36 > BV6 > BV48 > P25, which is consistent with the adsorption ability, the apparent rate constant as well as the mineralization yield. This tendency indicates that the intensity of surface hydroxyl groups of the BV samples is another significant factor that affects the photocatalytic activity. In photocatalysis reactions, surface adsorbed water or the surface hydroxyl group acts as the trap for the photogenerated hole, preventing electron–hole recombination, forming oxidative hydroxyl radicals, and subsequently oxidizing the adsorbed molecules on the substrate surface. For BV24, the high content of surface hydroxyl groups results in the highest adsorption capacity for IPA and the highest apparent rate constant.

3.7. DRIFT spectra analysis of IPA molecules

To further verify the effect of surface hydroxyl groups on the adsorption of isopropanol molecules, isopropanol interaction with the surfaces of BV samples, under darkness and visible-light illumination, was studied using in situ DRIFTS. The spectrum recorded upon the adsorption of isopropanol molecules at room temperature has three peaks, at 1383, 1252, and 1127 cm^{-1}, in the low wavenumber region assigned to the bending δ(CH) mode of IPA; in the high wavenumber region, a very intense band at 2978 and a weak band at 2888 cm^{-1} were observed, corresponding to the stretching ν(CH) mode of methyl groups of IPA. The intensities of C–H stretching and C–H bending bands reached a steady level

Table 2
Calculated various OH peaks in the IR spectrum (region from 3000 to 3700 cm^{-1}) obtained for BV samples at 250 °C.

Sample	Isolated-OH			Total area
	OH group chemically adsorbed at 3200 cm^{-1}	H bonded O–H stretching vibration at 3425 cm^{-1}	ν(OH) linear at 3687 cm^{-1}	
P25	2.30	8.46	0.10	10.86
BV6	20.84	152.72	65.25	238.81
BV12	47.79	300.70	111.20	459.69
BV24	40.37	410.87	105.50	556.74
BV36	24.87	257.96	86.60	369.43
BV48	10.98	102.61	38.50	152.09

Table 3
Calculated C–H bending band (peak at 2978 cm^{-1}) of IPA adsorbed on BV samples at adsorption equilibrium in the dark for 30 min and after 20 min of illumination.

Sample	C–H bending band (peak at 2978 cm^{-1}) of IPA		Difference between dark and illumination
	After 30 min of darkness	After 20 min of illumination	
BV6	4.61	0.03	4.58
BV12	5.79	0.04	5.75
BV24	7.05	0.46	6.59
BV36	5.10	0.04	5.06
BV48	3.93	0.31	3.62

after 30 min (results not shown). The ν(CH) mode of methyl groups (2978 cm^{-1}) was selected to represent the isopropanol molecules adsorbed on BV samples in the dark for 30 min. As shown in Fig. 9, the ν(CH) mode reached the highest intensity for BV24, indicating the highest adsorption equilibrium of IPA.

After 5 min of illumination of BV samples, an obvious decline in the intensity of the band centered at 2978 cm^{-1} was observed for all BV samples, indicating the decomposition of isopropanol molecules was proceeding as irradiated. The decreases are more intense for BV24 and BV12 compared to those of BV36, BV6, and BV48. The DRIFT spectra of the ν(CH) mode of methyl groups of adsorbed isopropanol molecules over BV samples after 20 min of illumination are shown in Fig. 10. The intensity of 2978 cm^{-1} was chosen again to represent the adsorbed IPA. To clarify the change of adsorbed isopropanol molecules, the area around the peak at 2978 cm^{-1} was calculated and presented quantitatively for comparison. The quantitative results of the intensity of 2978 cm^{-1} at adsorption equilibrium in the dark for 30 min and after 20 min of illumination are listed in Table 3. From Table 3, the highest adsorption amount of IPA in the dark is observed for BV24 and some amount of IPA is detected for the BV24 after 20 min of illumination. However, the highest reduction of the adsorbed IPA is obtained for BV24, which supplies the substantial proof of the best photocatalytic activity of BV24 among all the BV samples in the early stage. The above experimental results confirm that the surface hydroxyl groups present on BV samples are a crucial role in determining the adsorption ability and responsible for the performance of photocatalytic activity.

4. Conclusion

$BiVO_4$ photocatalysts were synthesized using a homogeneous co-precipitation process. All $BiVO_4$ samples exhibited a higher level of activity than that of a commercial TiO_2 photocatalyst (P25). Based on the apparent rate constant for the initial photodegradation of IPA and CO_2 production after long-term light irradiation, the BV24 samples exhibited the maximum visible-light photocatalytic activity. DRIFTS is shown to be useful in investigating in situ photoinitiated surface reactions due to good resolution and precise determination of chemical species appearing on the surface of photocatalysts. The DRIFT spectra make clarification on the correlation of the surface hydroxyl groups of $BiVO_4$ samples with adsorption and degradation of IPA. The rich surface hydroxyl groups imparted a high reactivity on $BiVO_4$ surface toward adsorbing IPA. These, along with a high degree of crystallinity, led to the highest photocatalytic efficiency of BV24.

Acknowledgements

We acknowledge the National Science Council, Taiwan, ROC, for providing research funding under grant NSC 98-2221-E-168-008. The authors would like to thank Professor Tai-Chou Lee, National Chung Cheng University, for assistance in XPS analysis.

References

[1] A. Kudo, Int. J. Hydrogen Energy 31 (2006) 197–202.
[2] S. Kohtani, S. Makino, A. Kudo, K. Tokumura, Y. Ishigaki, T. Matsunaga, O. Nikaido, K. Hayakawa, R. Nakagaki, Chem. Lett. 31 (2002) 660–661.
[3] J. Liu, H. Wang, S. Wang, H. Yan, Mater. Sci. Eng. B 104 (2003) 36–39.
[4] L. Ge, Mater. Chem. Phys. 107 (2008) 465–470.
[5] A. Zhang, J. Zhang, Spectrochim. Acta A 73 (2009) 336–341.
[6] T. Yang, D. Xia, G. Chen, Y. Chen, Mater. Chem. Phys. 114 (2009) 69–72.
[7] A. Zhang, J. Zhang, N. Cui, X. Tie, Y. An, L. Li, J. Mol. Catal. A: Chem. 304 (2009) 28–32.
[8] M. Gotic, S. Music, M. Ivanda, M. Soufek, S. Popovic, J. Mol. Struct. 744 (2005) 535–540.
[9] H.Q. Jiang, H. Endo, H. Natori, M. Nagai, K. Kobayashi, J. Eur. Ceram. Soc. 28 (2008) 2955–2962.
[10] D. Ke, T. Peng, L. Ma, P. Cai, P. Jiang, Appl. Catal. A: Gen. 350 (2008) 111–117.
[11] S. Kohtani, M. Tomohiro, K. Tokumura, R. Nakagaki, Appl. Catal. B: Environ. 58 (2005) 265–272.
[12] S. Kohtani, J. Hiro, N. Yamamoto, A. Kudo, K. Tokumura, R. Nakagaki, Catal. Commun. 6 (2005) 185–189.
[13] M. Long, W. Cai, J. Cai, B. Zhou, X. Chai, Y. Wu, J. Phys. Chem. B 110 (2006) 20211–20216.
[14] H. Xu, H. Li, C. Wu, J. Chu, Y. Yan, H. Shu, Mater. Sci. Eng. B 147 (2008) 52–56.
[15] H. Xu, H. Li, C. Wu, J. Chu, Y. Yan, H. Shu, Z. Gu, J. Hazard. Mater. 153 (2008) 877–884.
[16] H. Jiang, H. Endo, H. Natori, M. Nagai, K. Kobayashi, Mater. Res. Bull. 44 (2009) 700–706.
[17] P. Chatchai, Y. Murakami, S. Kishioka, A.Y. Nosaka, Y. Nosaka, Electrochim. Acta 54 (2009) 1147–1152.
[18] H. Jiang, M. Nagai, K. Kobayashi, J. Alloys Compd. 24 (2009) 821–827.
[19] H. Xu, C. Wu, H. Li, J. Chu, G. Sun, Y. Xu, Y. Yan, Appl. Surf. Sci. 256 (2009) 597–602.
[20] A.J. Maira, K.L. Yeung, C.Y. Lee, P.L. Yue, C.K. Chan, J. Catal. 192 (2000) 185–196.
[21] X. Wang, J.C. Yu, P. Liu, X. Wang, W. Su, X. Fu, J. Photochem. Photobiol. A: Chem. 179 (2006) 339–347.
[22] C.M. Huang, G.T. Pan, Y.C.M. Li, M.H. Li, T.C.K. Yang, Appl. Catal. A: Gen. 358 (2009) 164–172.
[23] C. Salazar, M.A. Nanny, J. Catal. 269 (2010) 404–410.
[24] G.T. Pan, C.M. Huang, L.C. Chen, W.T. Shiu, J. Environ. Eng. Manage. 16 (6) (2006) 413–420.
[25] F.D. Hardcastle, I.E. Wachs, J. Phys. Chem. 95 (1991) 5031–5041.
[26] J. Yu, A. Kudo, Adv. Funct. Mater. 16 (2006) 2163–2169.
[27] S. Tokunaga, H. Kato, A. Kudo, Chem. Mater. 13 (2001) 4624–4628.
[28] A. Kudo, K. Omori, H. Kato, J. Am. Chem. Soc. 121 (1999) 11459–11467.
[29] M.D. Hernández-Alonso, I. Tejedor-Tejedor, J.M. Coronado, M.A. Anderson, J. Soria, Catal. Today 143 (2009) 364–373.
[30] R. López, R. Gómez, M.E. Llanos, Catal. Today 148 (2009) 103–108.
[31] M.A. Aramendía, J.C. Colmenares a, A. Marinas, J.M. Marinas, J.M. Moreno, J.A. Navío, F.J. Urbano, Catal. Today 128 (2007) 235–244.
[32] C.M. Huang, L.C. Chen, K.W. Cheng, G.T. Pan, J. Mol. Catal. A 261 (2007) 218–224.
[33] G. Colón, M.C. Hidalgo, G. Munuera, I. Ferino, M.G. Cutrufello, J.A. Navío, Appl. Catal. B: Environ. 63 (2006) 45–59.
[34] M. Janus, A.W. Morawski, Appl. Catal. B: Environ. 75 (2007) 118–123.
[35] N.B. Colthup, L.H. Daly, S.E. Wiberley, Introduction to Infrared and Raman Spectroscopy, 3rd edition, Academic Press, Boston, 1990.
[36] J.M. Coronado, S. Kataoka, I. Tejedor-Tejedor, M.A. Anderson, J. Catal. 219 (2003) 219–230.